water

MDPI

Article

Improved Spectral Water Index Combined with Otsu Algorithm to Extract Muddy Coastline Data

Wei Tang [1], Chengyi Zhao [1,*], Jing Lin [1], Caixia Jiao [1], Guanghui Zheng [1], Jianting Zhu [2], Xishan Pan [3] and Xue Han [3]

[1] School of Geographical Sciences, Nanjing University of Information Science & Technology, Nanjing 210044, China; 20201211011@nuist.edu.cn (W.T.); linjingx0228@163.com (J.L.); jcx@nuist.edu.cn (C.J.); zgh@nuist.edu.cn (G.Z.)
[2] Department of Civil and Architectural Engineering, University of Wyoming, Laramie, WY 82071, USA; jzhu5@uwyo.edu
[3] Coastal Research Center of Jiangsu, Nanjing 210036, China; pxs0702@sina.com (X.P.); mathsocean@126.com (X.H.)
* Correspondence: zhaocy@nuist.edu.cn; Tel./Fax: +86-25-58235199

Abstract: Based on the spectral reflection characteristics analysis of the muddy coastline in Jiangsu, an improved spectral water index (*IWI*) combined with the Otsu algorithm is proposed to extract muddy coastlines from Landsat Operational Land Imager (OLI) images. The IWI-extracted coastline results are compared with those extracted by the modified normalized difference water index (*MNDWI*), normalized difference water index (*NDWI*), enhanced water index (*EWI*), revised normalized different water index (*RNDWI*) and automated water extraction index (*AWEI*). The results show that the *IWI* is not affected by tidal conditions or sand content in the water, can reduce the "salt-and-pepper" phenomenon in the Otsu algorithm classification, can accurately identify water boundaries and can extract silty mudflats and marine buildings with high accuracy. It can also significantly increase the degree of automation of coastline extraction. The *IWI* combined with the Otsu algorithm demonstrates high accuracy of over 84% in the extraction muddy coastline data with one-pixel tolerance, which is twice as accurate as other indices. The accuracy of extraction for all other types of coastlines is over 81%. Therefore, the *IWI* index combined with the Otsu algorithm is reliable for studies of sea–land processes and coastline evolutions.

Keywords: coastline extraction; muddy coast; spectral reflectance; spectral index; Otsu algorithm

Citation: Tang, W.; Zhao, C.; Lin, J.; Jiao, C.; Zheng, G.; Zhu, J.; Pan, X.; Han, X. Improved Spectral Water Index Combined with Otsu Algorithm to Extract Muddy Coastline Data. *Water* **2022**, *14*, 855. https://doi.org/10.3390/w14060855

Academic Editor: Rafael J. Bergillos

Received: 19 January 2022
Accepted: 8 March 2022
Published: 9 March 2022

1. Introduction

A coastline is a geomorphological signature of sea–land interactions, and has been identified by the International Geographic Information Committee (IGDC) as one of the 27 most important land surface features [1]. Coastline variability is a representation of the evolution of coastal zone resources and environmental ecosystems under climate change, sea level change and sea–land interactions, and is also an integral reflection of human influence and modification of the natural environment, as well as adaptation and response to climate change [2–6]. The methods of coastline extraction include traditional mapping and remote sensing. With the traditional mapping method it is difficult to obtain large-scale coastline images in a short period of time, and dynamic monitoring of coastlines is not feasible [7]. Remote sensing image-based coastline extraction is not restricted by the weather, surface, sea conditions or geographical environment, and has the ability for fast, flexible and continuous monitoring [8]. With the continuous improvement of the spatial, temporal and radiometric resolutions of satellite sensors, the image processing techniques for coastline extraction based on multi-source remote sensing information are becoming more diverse. The threshold method based on spectral

bands is one of the most important methods [1], which focuses on setting thresholds to separate sea and land areas to extract coastlines by enhancing the differences between the target object and background. The spectral index algorithm is sensitive to waveband information [9–11], and the image processing requires the selection of a suitable spectral index based on the absorption characteristics of the target object to the spectrum. McFeeters [12] constructed the *NDWI* by analyzing the spectral characteristics of water bodies and vegetation, which can effectively suppress vegetation information and distinguish water bodies from vegetation and mountain shadows, but ignored the influence of soil, buildings and shadows. For the extraction of urban water bodies, Xu et al. [13] constructed the *MNDWI* by analyzing the spectral features of buildings and enhancing the contrast between water bodies and buildings. To reduce the influence of mixed image element factors, vegetation and mountain shadows, Cao et al. [14] constructed the *RNDWI* to extract the water surfaces of reservoirs. Yan et al. [15] constructed the *EWI* to effectively distinguish semi-dry rivers from background noise. Feyisa et al. [16] constructed the *AWEI* to improve the automatic classification of shaded and low-reflectance water bodies. Other studies also used the above spectral indices to extract coastlines. Sheng et al. [17] used the *NDWI* to extract vegetated coastlines in the Strait of Malacca. Sandra [18] used an improved index to extract bedrock coastlines in the Spanish delta. Du [19] used the *MNDWI* to extract different types of coastlines in small areas of lagoons along the coast of Venice in Italy. To address the uncertainty in extracting water bodies or coastlines from different regions using the spectral water index, Wu et al. [20] analyzed the extraction ability levels of various spectral indices for water bodies in silty shores in the Yellow River Delta and showed that the $AWEI_{nsh}$ (one of the formulae of *AWEI*, the other being $AWEI_{sh}$) had the best extraction effect and that the *MNDWI* had a higher leakage rate for seawater than other indices. Zhang et al. [21] extracted the muddy coastline of Shandong Peninsula using a different extraction method from that used to extract silty and bedrock coastlines, and the results showed that the average error of the extracted muddy coastline was 21%, much higher than the average error for other coastline types. However, few studies have been conducted on the extraction methods for muddy coastlines with average tidal differences greater than 4 m, such as the threshold method and edge detection method [22,23]

The muddy coastline areas in the Jiangsu Sea are more complex than other types of coastlines, since they are influenced by the Yangtze River, the Yellow River, and the Huaihe River, which carry sand and form silty mudflats. The maximum tidal difference in the Jiangsu Sea is more than 6 m and the average tidal difference between the north and south is more than 3 m, while the coastline is particularly influenced by the tides [24]. The silty mudflats, which "appear and disappear", are the most tidally influenced areas [25,26], in which water remains after low tide, with a large number of mixed pixels of water and mudflats and complex spectral properties. This leads to similarities between the spectral reflectance values of silty mudflats and water. Therefore, the applicability of the previous spectral water index is reduced, affecting the subsequent identification and classification. In addition to the above factors, the high sediment content of water bodies is another major characteristic that differs from inland water bodies. The coastline types in Jiangsu are diverse and complex, and there is an urgent need to explore extraction methods for complex typical coastlines to improve the extraction accuracy, especially for muddy coastlines.

This study attempts to develop a new extraction method for muddy coastlines in Jiangsu based on improved spectral indices combined with the Otsu algorithm [27] using Landsat-8 OLI images, and to compare it with the five most commonly used spectral indices (*MNDWI, NDWI, EWI, RNDWI* and *AWEI*) to explore the extraction of complex coastlines. The results of this study will provide a basis for the long-term monitoring of complex coastlines and a more improved understanding of sea–land processes and coastline evolution.

2. Study Area and Data Sources

2.1. Study Area Overview

Jiangsu is located on the shores of the Yellow Sea and the East China Sea (see Figure 1A) and has the largest muddy coastline in China, which is unique globally. Figure 1a,b and 1c represent northern, central and southern Jiangsu coast respectively. The Jiangsu offshore area has a regular semi-diurnal tide with the largest tidal range in the central sea, forming a decreasing trend from the central to the north and south. In the main intertidal tidal channels, the maximum tidal speeds reach 3 m s^{-1}. Due to the gentle tidal mudflats, the strongest wave height is less than 1 m in winter, while in other seasons the wave height is only about 0.5 m [28]. The coastline of Jiangsu is continuously silted by the transported sediment from the Yangtze and Yellow Rivers, and after the shift of the Yellow River to the north, the coast shows erosion in the north and siltation in the south. With the lack of large amounts of sediment, the middle section is subject to the intersection of the South Yellow Sea's rotating tidal wave system and the East China Sea's advancing tidal wave system, resulting in the formation of the current large-scale underwater radial sandbars. The coastline types of Jiangsu are complex, with the Lianyungang section dominated by bedrock and sandy coastlines, the Yancheng section dominated by chalky-silt coastlines and the Nantong shore section dominated by polder and silt coastlines [29]. Overall, the silt shore type accounts for about 93% of the province's coastline length [30]. Since the 1990s, the coastal silty mudflats resources have been mainly used for aquaculture and industrial port construction [31], and the coastline has since changed considerably.

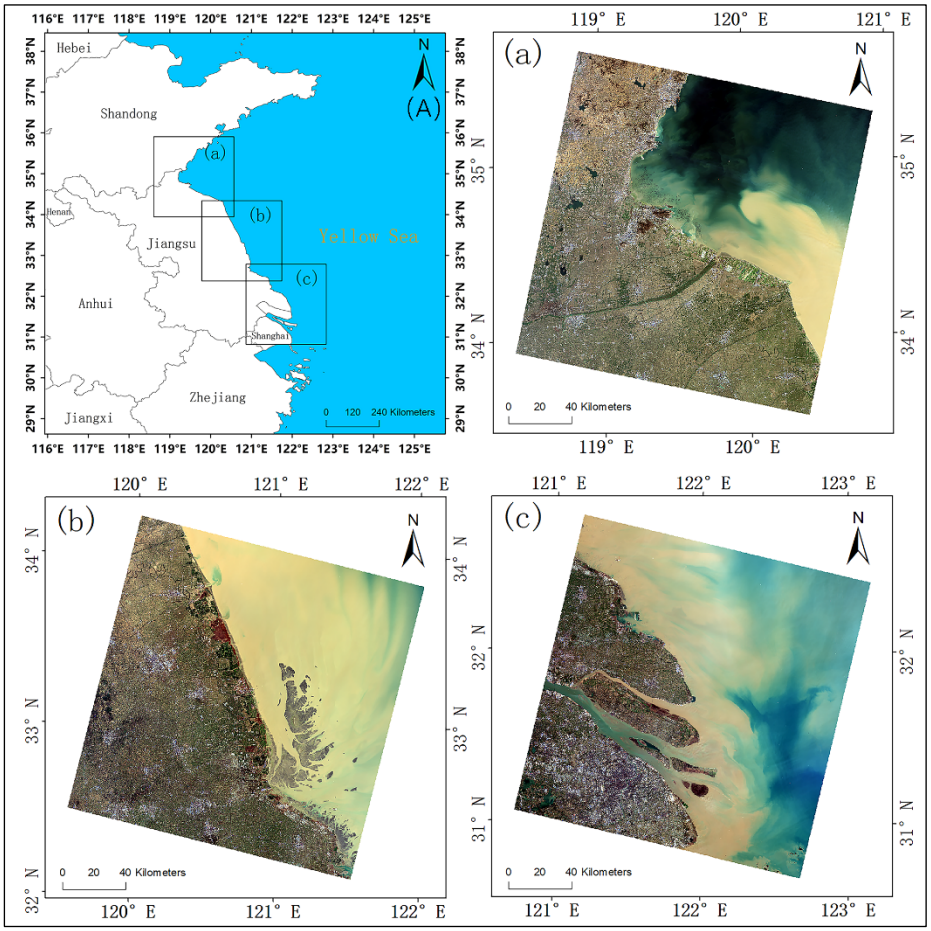

Figure 1. Schematic diagram of the study area: (A) study area and image coverage location map (a) northern Jiangsu coast; (**b**) central Jiangsu coast; (**c**) southern Jiangsu coast. All images correspond to the data in Table 1, while the path and row numbers are 120036, 119037 and 118038.

2.2. Data Sources

The study is based on the Landsat-8 OLI surface reflectance (SR) data provided by the Google Earth Engine platform as the base data (see Table 1) [32]. The SR data were pre-processed with geometric and atmospheric correction and with quality assurance for the quality assessment bands [33]. The SR data were acquired by a single-pass algorithm with atmospheric correction, taking into account not only the effect of surface-specific radiance but also atmospheric radiation. The Landsat-8 OLI multispectral band has a spatial resolution of 30 m and a re-entry period of 16 days. Since clouds can obscure feature information and affect the extraction of coastlines, images with low cloud cover were preferred [34]. The images used in this study all had less than 3% cloud cover.

Table 1. Images used in the study.

Landsat Sensor	Path/Row	Image Time	Tide
OLI	p120/r036	2017/02/11	High
OLI	p119/r037	2018/02/23	Low
OLI	p118/r038	2020/02/22	High

3. IWI Index Construction and Water Extraction Method

3.1. Analysis of Spectral Characteristics of Ground Objects

The core of this study is the distinction between open water (marine) and land and the extraction of coastlines. The focus is on the different coastal types, which are classified based on important features, such as low-sediment water far from the coast, high-sediment water near the coast, silty mudflats and coastal vegetation, while other feature such as arable land, built-up areas, roads and mountains are classified as land features. The spectral differences between the different types of coastal features are analyzed to assist in subsequent studies.

Based on the above classifications, pure images of relevant features are selected from the images described in Table 1. More than 10,000 pixels of each feature are selected and the average reflectance of each band was calculated, as shown in Figure 2. As can be seen from Figure 2, the reflectance of water with high and low sediment content varies similarly from the visible band (0.450–0.680 um) to the near infrared band (0.680–0.885 um), gradually increasing in the visible band, reaching a maximum in the green band and then decreasing in the near infrared band, reaching almost zero near the shortwave infrared band. This is different from the variations in clear water, for which reflectivity is approximately 4% and may be related to the turbidity of the sand content of the water body [35], in which the increase in sediment content causes an increase in reflectance. Clear water has a strong absorption capacity for incident energy and has a low reflectance over most of the sensor's wavelength range. There is a tendency for the absorption to increase with increasing wavelength in clear water. As shown in Figure 2, low-sediment water can be approximated as a clear body of water with a reflectance of approximately 5% in the visible wavelength range, dropping to 2.5% in the red band range; beyond the visible range, over 98% of the energy incident on the clear water is absorbed. In contrast, the reflectance range of water with a high sediment content near the Jiangsu coast is about 10% to 15% in the near infrared band, almost four times the reflectance of clear water. The reflectance of the silty mudflats varies slightly across all wavelengths, with a peak of less than 5%, while the reflectance fluctuates between 5% and 10% and the trend is highly similar to the water bodies. Coastal vegetation has low reflectance in the visible band, increases to a maximum in the near infrared band as the wavelength increases and then decreases in the shortwave infrared band, with significant differences from other features. The land type contains a large variety of features indicated by much greater variations in reflectance in different bands, with images rising and falling steeply.

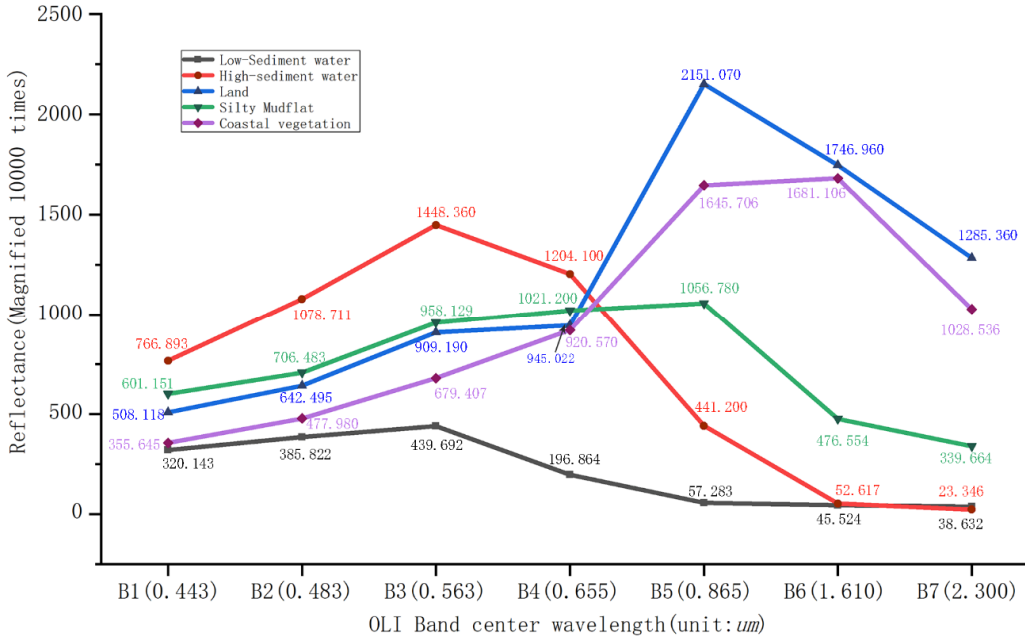

Figure 2. Average spectral reflectance of typical features in the study area.

3.2. IWI Index Construction

The ratio method determines the ratio of the strongest reflection band over the weakest reflection band of the target object. Through the ratio calculation, the difference between the target object and the background is amplified. The *NDVI, NDWI and MNDWI* can be considered as representatives of the ratio index (see Table 2 for formulates). The blue band has a certain penetration effect on water, which can be used to obtain underwater information [36]. At the same time, it can be seen from Figure 2 that the blue band still has relatively high reflectivity of sediment water. Previous studies did not consider the blue band. For this reason, the *IWI* proposed in this study uses the four spectral bands of Landsat-8 OLI to construct a new index (Equation (1)). The new index, *IWI*, combines the blue and green bands to form a high-reflectance band combination and combines the short-wave infrared band to form a low-reflectance band combination. The square of the ratio of these two combinations is then used to highlight the separability of sediment water from silty mudflats, as expressed in Equation (1) below:

$$IWI = [(\rho b2 + \rho b3 - \rho b6 - \rho b7)/(\rho b2 + \rho b3 + \rho b6 + \rho b7)]^2 \quad (1)$$

where ρ is the reflectance and $b2$, $b3$, $b6$ and $b7$ are the OLI Blue, Green, SWIR1 and SWIR2 bands, respectively.

The reflectance spectral properties of silty mudflats are more similar to those of sediment water, which are often difficult to distinguish. Equation (1) can enhance the differences between silty mudflats and sediment waters (see Table 3), can increase the variance between classes and to make the thresholds obtained by the Otsu algorithm more accurate. The *IWI* is constructed according to the characteristics of high reflectivity of sediment waters in blue and green bands to eliminate the misclassification caused by threshold classification when the residual water bodies of silty mudflats are calculated as positive based on the ratio index. It can increase the difference between sediment water and other non-water pixels (e.g., silty mudflats) so that the reflectivity of the residual water bodies of the silty mudflats will be close to the water bodies. The most complex variation in silty mudflats is found in different tidal scenarios, and this difficulty has been overlooked by previous approaches that have chosen high tide images and cannot be applied to other scenarios.

The reflectance of the silty mudflats is close to but lower than that of the sediment waters in all bands. The values obtained using the *MNDWI* and *NDWI* formulae may be either positive or negative, which can be avoided by using the square operation in Equation (1). The algorithm no longer discriminates between types based on the calculated positive and negative values, and the square operation amplifies the difference so that the reflectance of sediment waters remains high and the reflectance of silty mudflats is much lower, forming a bimodal distribution. As in Table 3, low-sediment water and high-sediment water are grouped into one class, and other features are grouped into one class, so the variance between the two classes needs to be increased. Therefore, using the data in Table 3 as an example, the silty mudflats of *MNDWI*, *RNDWI*, *EWI*, $AWEI_{sh}$ and *NDWI* have similar differences in values to sediment water or land–coastal vegetation, which may lead to some misclassification, while the silty mudflat of *IWI* is far from sediment water and land–coastal vegetation is more likely to provide a better Otsu threshold.

Therefore, the expected results of the *IWI* equation are as follows: (1) the silty mudflats 'disappear' at high tide, enhancing the separability of sediment waters from coastal vegetation, buildings and other pixels; (2) the silty mudflats 'appear' at low tide, enhancing the separability of sediment waters from silty mudflats. Table 2 compares the *IWI* with several other water indices, where the *AWEI* is a non-ratio index and all others are ratio indices.

Table 2. Comparison of various spectral water indices.

Index's Name	Formula
IWI	$((\rho b2 + \rho b3 - \rho b6 - \rho b7)/(\rho b2 + \rho b3 + \rho b6 + \rho b7))^2$
MNDWI	$(\rho b3 - \rho b6)/(\rho b3 + \rho b6)$
$AWEI_{nsh}$	$4 \times (\rho b2 - \rho b5) - (0.25 \times \rho b4 + 2.75 \times \rho b7)$
$AWEI_{sh}$	$\rho b1 + 2.5 \times \rho b2 - 1.5 \times (\rho b4 + \rho b5) - 0.25 \times \rho b7$
RNDWI	$(\rho b6 - \rho b4)/(\rho b4 + \rho b6)$
EWI	$(\rho b3 - \rho b4 - \rho b6)/(\rho b3 + \rho b4 + \rho b6)$
NDWI	$(\rho b3 - \rho b5)/(\rho b3 + \rho b5)$

Here, ρ is the reflectance of each band of the multispectral Landsat8 OLI and bi (i =1...,7) is each band of the multispectral spectrum.

Table 3. Calculation results of each index are based on Figure 2.

Index's Name	Low-Sediment Water	High-Sediment Water	Land	Silty Mudflat	Coastal Vegetation
IWI	0.664184	0.886677	0.104329	0.116950	0.161128
MNDWI	0.812356	0.929890	−0.315410	0.335666	−0.424360
$AWEI_{nsh}$ [1]	0.115870	0.218482	−0.980530	−0.259060	−0.772950
$AWEI_{sh}$ [1]	0.089382	0.098988	−0.285110	−0.083450	−0.255600
RNDWI	−0.624370	−0.91626	0.297899	−0.363640	0.292325
EWI	0.289268	0.070846	−0.495060	−0.219730	−0.585860
NDWI	0.769473	0.533013	−0.405810	−0.048960	−0.415590

[1] The calculation is divided by 10,000.

3.3. IWI Index Combined with Otsu Algorithm for Water Extraction

The extraction of water bodies based on spectral indices requires a threshold to divide the image into two classes, land and water bodies. The problem is that the threshold for the spectral index is not constant but varies with land cover. The Otsu algorithm [25] is based on an automatic selection of the optimal threshold from the grey-scale image to maximize the differences between classes. Previous studies have shown

that the Otsu algorithm could be successfully applied to the separation of water bodies from the Landsat imagery [37]. The optimal threshold t* in the range a~b (−1 ≤ a ≤ b ≤ 1) is determined by the following algorithm [25]:

$$\begin{cases} \sigma^2 = P_{nw} \cdot (M_{nw} - M)^2 + P_w \cdot (M_{nw} - M)^2 \\ M = P_{nw} \cdot M_{nw} + P_w \cdot M_w \\ P_{nw} + P_w = 1 \\ t^* = \text{Arg} \max\limits_{a \le t \le b} \{P_{nw} \cdot (M_{nw} - M)^2 + P_w \cdot (M_{nw} - M)^2\} \end{cases} \quad (2)$$

where σ is the inter-class variance of non-water and water pixels. P_{nw} denotes the probability that a pixel belongs to a non-water pixel and P_w denotes the probability that a pixel belongs to a water pixel. M_{nw} and M_w denote the means of all non-water pixels and all water pixels, respectively, and M is the mean of the whole image. Pixels with values greater than or equal to the optimal threshold are classified as water and calculated as 1; conversely, pixels are classified as non-water pixels and calculated as 0. Note that water and non-water categories are assigned values opposite to those described above in the *RNDWI* (i.e., 0 for water and 1 for non-water).

3.4. Coastline Extraction and Accuracy Evaluation

Based on the results of the above water body extraction, the coastline was determined by the vectorized water–land boundary line, and the estuarine coastline was determined as the coastline connection at the maximum estuarine widening according to Hou et al. [38], which occurred after vectorization. The outermost edge vector was taken as the shoreline to be determined and the estuarine shoreline was truncated at the outermost edge inflection point, after which the two truncation points were joined to complete the estuarine shoreline connection. To quantify the accuracy of coastline extraction, the coastline was manually interpreted using the higher-resolution Sentinel-2 images taken on the same day as the validation coastline, with a spatial resolution of 10 m in the visible band of Sentinel-2. By selecting images taken on the same day, the time difference between the two images at the corresponding locations from different sensors is about 15–20 min, so that the corresponding image element feature type can be considered unchanged.

4. Analysis and Evaluation of Results

4.1. Comparison of Extraction Results for Open Water Bodies (Marine)

Figure 3 shows the results of the classification of water bodies (marine) and other features calculated by each index (Table 2) and the Otsu algorithm for different tidal scenarios. There are areas of overlap between Figure 3a,b and between Figure 3b,c, with different tidal scenarios and different coastline locations. Figure 3a shows the Otsu results for each index from Figure 1a, with a few misclassified areas of deep water in the *IWI* and a large number of misclassified areas of highly sandy water in the *NDWI* and $AWEI_{sh}$. The *IWI*, despite the above misclassifications, has better results in removing mountain shadows and identifying features such as offshore structures. Figure 3b shows the Otsu results for each index in Figure 1b with radial sandbars 'visible' in this image and muddy coastlines as the dominant coastline type. The indices that are better identified for the silty mudflats are the *IWI*, *MNDWI* and *RNDWI*. The radial sandbar is not correctly identified in the *NDWI* results and a large area of the inshore is misidentified. Therefore, the *IWI* has a higher ability to identify open water bodies (marine) for different tidal conditions.

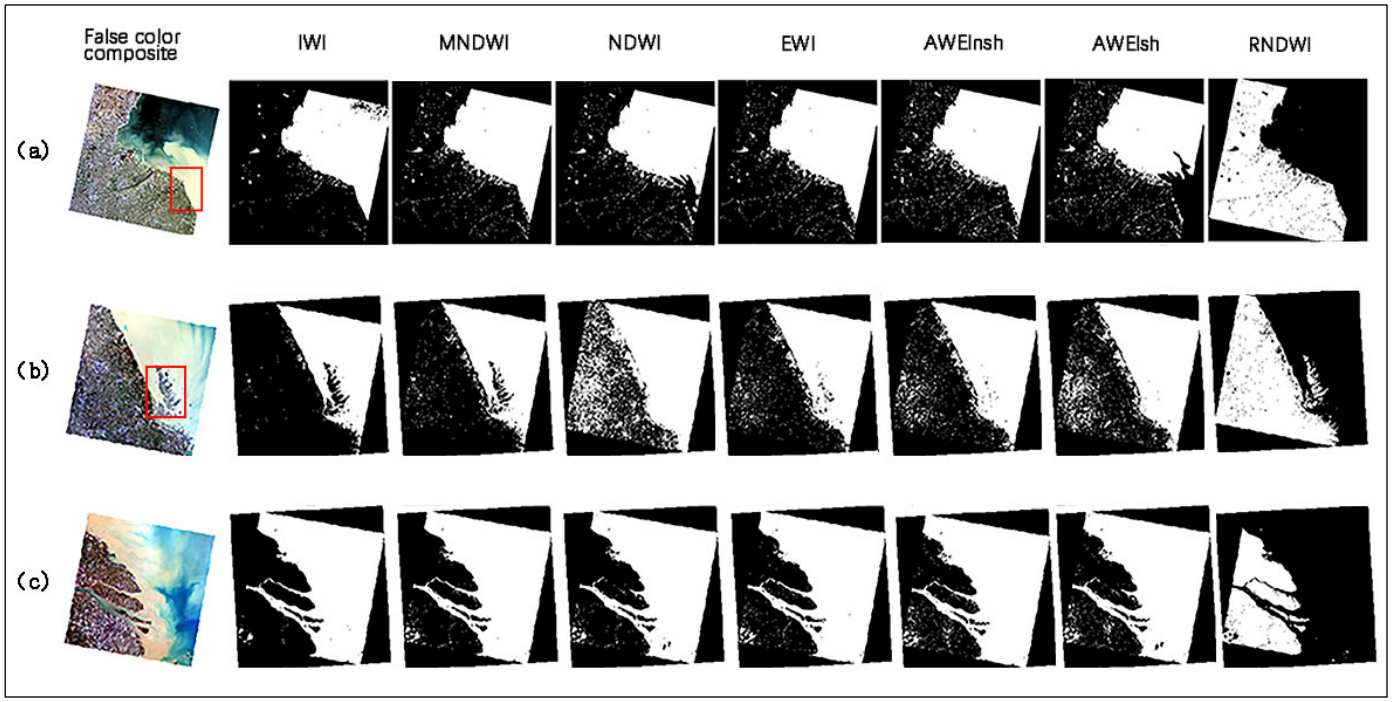

Figure 3. Otsu classification images of each index, whereby the red box in the diagram shows the misclassified areas of the Otsu classification; (**a**–**c**) correspond to the positions in Figure 1a, 1b and 1c.

This study differs slightly from the general water body extraction studies in that the accuracy of the inland water body extraction is not considered, and emphasis is placed on the extraction of water bodies at the intersection of open water bodies (marine) and land. Figure 4 shows in more detail the results of *IWI* and other indices for the extraction of water bodies at the interface between land and sea. Figure 4a,d,g shows the artificial shore area, with the results demonstrating that the *IWI* has the best clarity and continuity for artificial structures, while the *AWEI* is not successful in identifying this area. Figure 4b shows the sandy shore area, where the water contents in sand and gravel cause small numbers of classification errors in the *MNDWI*, *EWI*, *AWEI* and *RNDWI*. Figure 4c–f shows the results for the silty shore, where the *MNDWI*, *EWI* and *AWEI* have almost zero ability and the *MNDWI* and *RNDWI* also have a large number of missed areas, indicating low applicability, while the *IWI* better identifies the silty mudflats. Figure 4g,h shows the enclosed mariculture shore with a small coast extent of only 1–2 pixels, where the so-called "salt-and-pepper phenomenon" of misclassification can greatly affect the identification of the correct location of the coastline. The results, however, show that the *IWI* index can avoid this phenomenon very well.

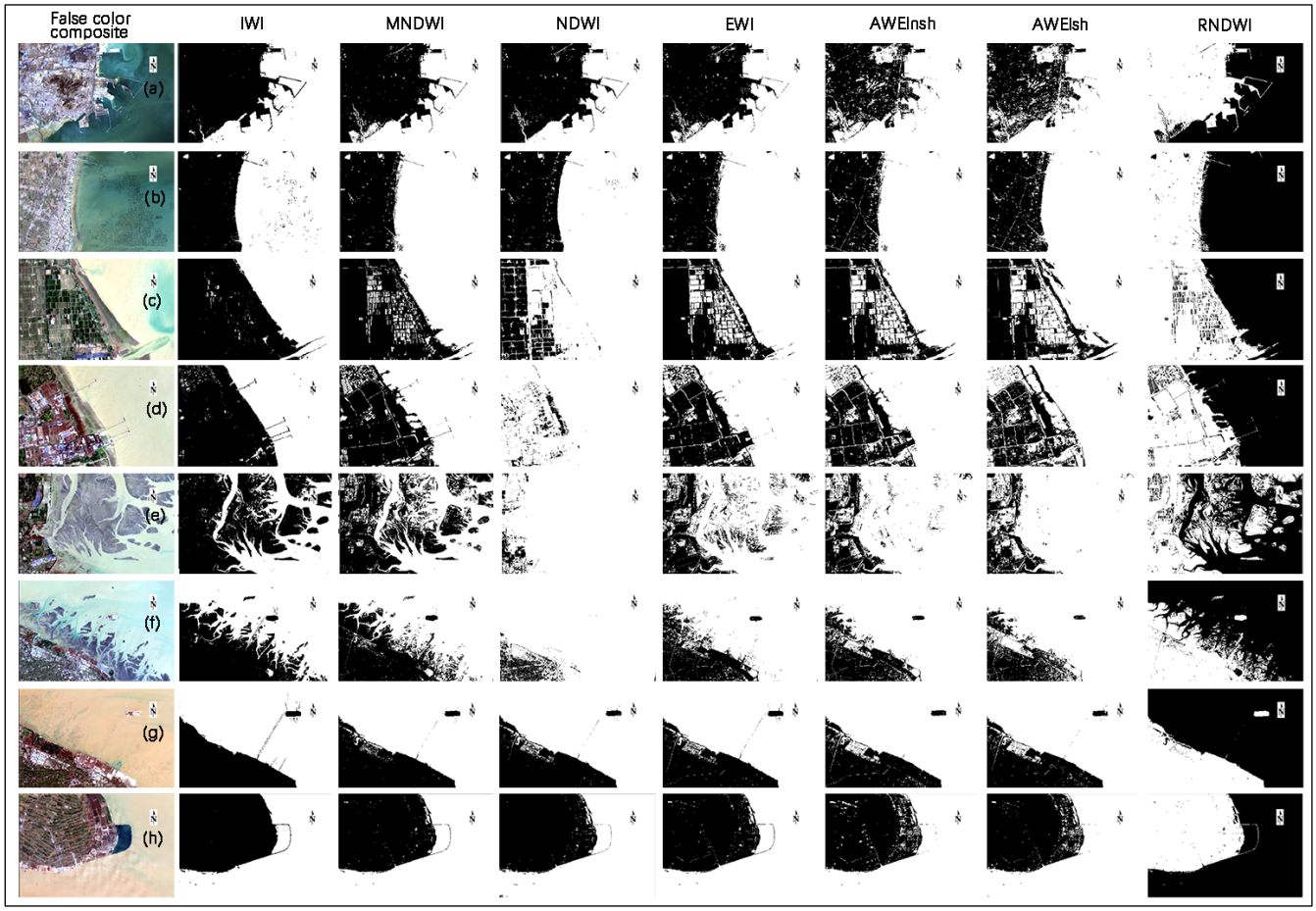

Figure 4. Diagram of partial results of different coastline types extracted for each index: (**a**,**d**,**g**) the artificial shore area; (**b**) the sandy shore area; (**c**,d,e,**f**) the silty shore area; (**g**,**h**) the enclosed mariculture shore.

4.2. Accuracy Analysis of Coastline

The results of the partial shoreline validation in Table 4 show that the *IWI* has high accuracy for different shoreline types, and the accuracy is higher than 77% with one pixel as the evaluation index, while the *NDWI* has the worst result with an accuracy of 0 in Figure 4c–f. In general, the differences in accuracy between the indices for the silty mudflats are large, and the differences in accuracy between the indices for the artificial shoreline are small.

Table 4. Accuracy analysis of the local coastline results (%) for different indices.

Index's Name	Validation Distances (m)	Figure 4a	Figure 4b	Figure 4c	Figure 4d	Figure 4e	Figure 4f	Figure 4g	Figure 4h
IWI	0–30	91.84	82.63	77.79	91.45	83.47	92.86	87.56	99.12
	0–60	96.46	84.46	84.54	94.89	86.45	95.45	91.36	100.00
	0–90	98.31	90.46	91.97	98.71	89.92	98.57	100.00	100.00
EWI	0–30	89.55	2.44	20.47	1.81	11.21	7.13	1.45	94.63
	0–60	93.46	5.63	24.91	3.45	24.63	9.45	67.32	97.48
	0–90	95.73	7.45	30.47	9.47	32.66	11.78	84.56	99.29
MNDWI	0–30	84.69	1.30	21.35	19.54	58.13	52.68	57.41	92.66
	0–60	91.79	4.62	26.41	24.23	64.18	57.89	76.79	98.45
	0–90	93.41	8.33	32.45	30.22	74.55	61.42	84.63	99.34
	0–30	84.77	57.24	0.00	0.00	0.00	0.00	0.47	76.85

NDWI	0–60	91.93	64.15	0.00	0.00	0.00	0.00	64.48	88.48
	0–90	96.42	74.31	0.00	0.00	0.00	0.00	81.60	93.45
	0–30	33.64	1.48	9.43	2.04	7.43	8.65	1.78	17.63
$AWEI_{nsh}$	0–60	70.49	3.51	15.74	8.47	15.76	9.45	46.96	26.36
	0–90	81.33	8.47	24.69	9.45	19.48	10.71	62.01	37.44
	0–30	78.38	1.72	18.49	21.46	62.13	57.43	60.47	91.46
RNDWI	0–60	82.46	4.12	23.41	27.63	72.46	63.47	64.79	94.21
	0–90	88.63	9.54	26.48	31.01	78.14	71.13	68.47	98.43
	0–30	24.95	9.46	21.36	14.32	6.77	0.00	0.58	64.57
$AWEI_{sh}$	0–60	56.64	30.46	25.46	19.76	10.65	0.00	58.46	74.93
	0–90	76.49	50.84	49.78	26.87	11.24	0.00	70.42	82.36

Figure 5 shows a comparison of the coastline results extracted by each index. Parts (Figure 5a–c) of the figure correspond to the coastline results extracted by each index based on the images in Figure 1a–c. Figure 5b shows the most significant difference in the coastline, with the continuity being greatly challenged in the extraction of the coastline. Figure 5a is similar to Figure 5b,c has the least differences and most consistent extraction results among the indices. The differences between results are due to the differences in sensitivity of the silty mudflats and offshore artificial buildings to different combinations of spectral bands. A comparative analysis of the coastline extraction results in the overlapping areas (Figure 5A–D) shows that the differences in the extraction of coastlines among the indices are smaller at high tide than at low tide. There is little difference in the extraction results of multiple indices in high tide area (Figure 5A,D), and there is great difference in the extraction results of multiple indices in the low tide area (Figure 5B,C). At low tide, the silty mudflats are exposed but the muddy coast is not well identified, except by the *IWI*.

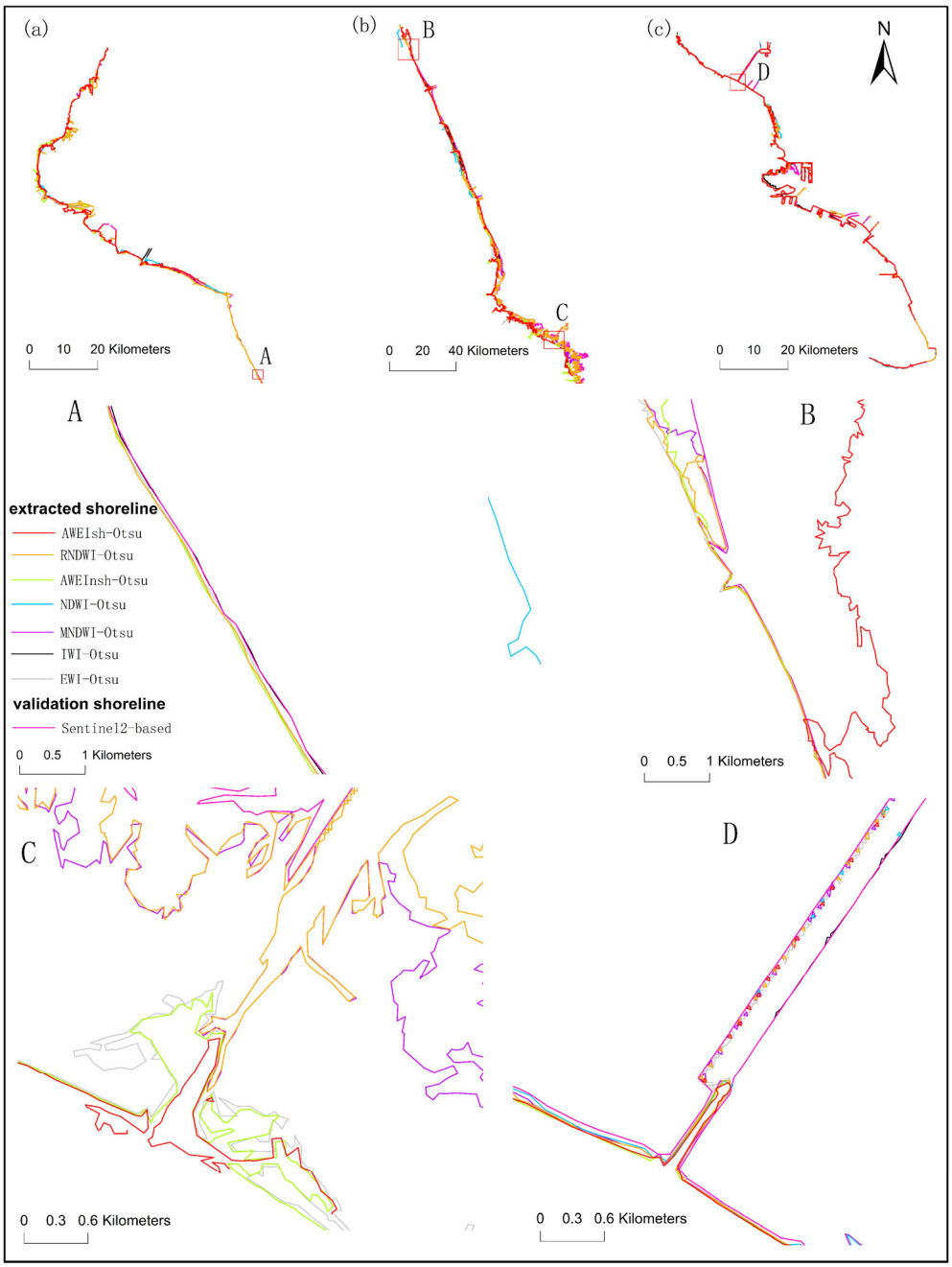

Figure 5. Comparison image of extracted coastline results: (**a**–**c**) the result maps of northern, central and southern coastlines of Jiangsu extracted using various methods; enlarged maps of local results, where (**A**–**D**) are the overlapping areas

In order to quantitatively evaluate the accuracy of the coastline extraction by each index, the validation coastline interpreted by Sentinel-2 was used to calculate the ratio of the extracted coastline within the validation coastline using the widths of one pixel, two pixels and three pixels of Landsat-8 OLI as error tolerances. The calculated ratio (in %) was used as a proxy for the accuracy of the extracted coastline. The validation results are presented in Table 5. Figure 6 shows the shoreline local validation results.

Table 5. Accuracy analysis of the coastline results (%) for different indices.

Index's Name	Figure 1a (0–30 m)	Figure 1a (0–60 m)	Figure 1a (0–90 m)	Figure 1b (0–30 m)	Figure 1b (0–60 m)	Figure 1b (0–90 m)	Figure 1c (0–30 m)	Figure 1c (0–60 m)	Figure 1c (0–90 m)
IWI	81.63	92.74	97.36	84.61	86.77	94.72	85.86	89.47	91.45
EWI	59.00	65.55	69.29	7.18	12.97	15.13	55.25	76.91	84.23
MNDWI	55.44	66.06	71.62	38.21	48.03	52.68	50.69	72.40	78.37
NDWI	58.03	63.46	66.77	0.00	0.04	0.13	44.78	67.73	76.54
$AWEI_{nsh}$	25.69	43.41	50.17	7.04	12.81	14.65	17.65	45.75	55.94
RNDWI	60.62	70.60	76.13	40.41	52.30	57.43	46.36	66.86	73.61
$AWEI_{sh}$	21.30	35.44	40.88	8.81	15.74	19.67	23.88	50.24	61.99

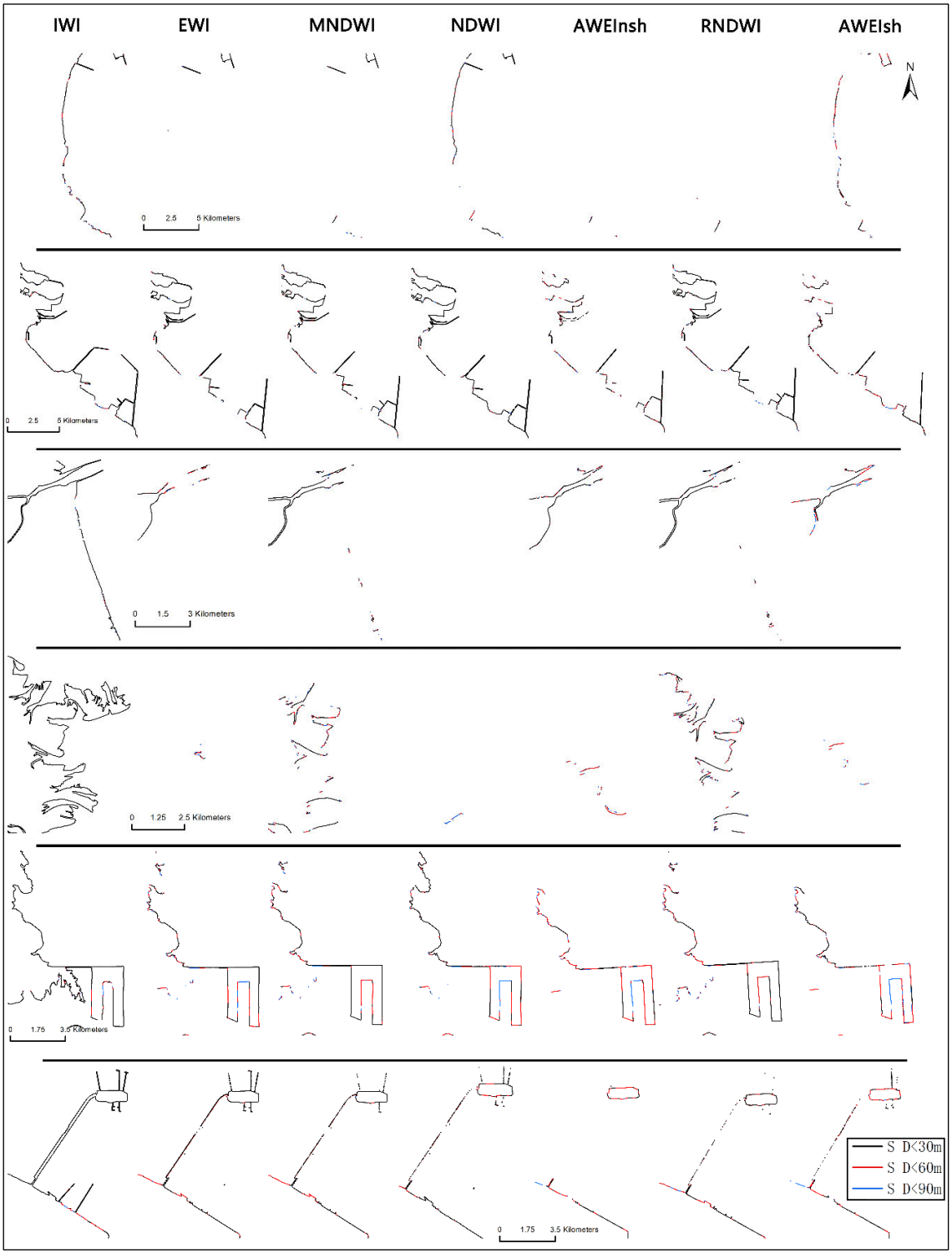

Figure 6. Image of shoreline local validation results, in descending order of dimensionality. The legend S D (coastline distance) indicates the distance between the extracted coastline and the validation coastline; black, red and blue represent the different validated coastline distances.

From the validation results in Table 5, we can conclude that the coastline accuracy extracted by the *IWI* with the Otsu algorithm exceeds 81% in all three scenarios compared to the validation coastline, while the accuracy exceeds 91% for the three-pixel tolerance for all three images, which is the highest accuracy among the indices. The lowest accuracy of almost zero comes from the coastline of the *NDWI*-extracted image in Figure 1b. For the image in Figure 1a for the one-pixel tolerance, the *RNDWI*- and *MNDWI*-extracted

coastline result is the second highest after the *IWI* at approximately 60%. For the image in Figure 1b, all indices are below 50% accuracy, except for the *IWI* for the one-pixel tolerance. For the image in Figure 1c, the *EWI*-, *MNDWI*- and *NDWI*-extracted coastline results have accuracy levels above 76% for the three-pixel tolerance. Overall, with the exception of *IWI*, the response of the index to water varies considerably under different tide and sediment conditions. Sensitivity can be defined as the influence of tide and water turbidity when the index identifies a water body, which is the opposite of the accuracy. The sensitivity can be ranked as *IWI* < *MNDWI* < *RNDWI* < *EWI* < *AWEI* < *NDWI* in this study.

5. Discussion

Landsat 8-OLI is the latest satellite of the Landsat series launched specifically for global land resource monitoring, which can be used to monitor coastline changes and support the studies of coastal evolutions and sea–land interactions. The Jiangsu coast has the world's unique radial sandbars and a wide intertidal zone. The spectral reflectance of the silty mudflats from visible band to shortwave infrared band wavelengths is similar to that of the water body, and the difference in reflectance of each band is as small as 0.05. The indices developed in previous studies did not take into account the influence of the silty mudflats on the extracted coastline, resulting in poor results and an inability to extract the muddy coastline under various tidal conditions. To better identify silty mudflats and extract coastlines under different tidal conditions, in this we study constructed a new spectral index to improve the extraction accuracy of muddy coastlines based on the analysis of spectral characteristics of nearshore features such as silty mudflats, vegetation, land and water bodies. The blue band was added to form a combination of high-reflectivity and low-reflectivity bands using a ratio-based algorithm. Silty mudflats and sandy coastlines are often inundated by water, and water bodies may remain at low tide, resulting in frequent misclassification by remote sensing. Therefore, the algorithm constructed in this study adds the blue band, which has a short electromagnetic wavelength; contains high energy; and has strong penetrating power and the ability to penetrate the water body to obtain underwater features. The improved index enhances the differences between sediment waters and silty mudflats. The corresponding algorithms based on the improved index are more suitable for the classification of features with flat and changing spectra.

In this study, we used the global automatic threshold algorithm (i.e., Otsu algorithm) to classify water bodies and non-water bodies. The *IWI* algorithm focuses on the differences between silty mudflats and sediment water bodies, and the difference between the calculated results was greater than 0.5, which is generally bimodal and useful for accurate classification of the global automatic threshold. The applicability to other features is, however, reduced. In addition, the global threshold may cause some clear water bodies with very low reflectivity to be misclassified. It is, therefore, helpful if a chunked threshold is used for the classification of clear water bodies in very small areas, and the size of the sliding window needs to be properly determined. However, the study area of Jiangsu offshore water bodies in this study is turbid, with high suspended sediment content, and the *IWI* calculation value of offshore suspended sediment waters is high, so the global threshold has a low impact on the extraction of offshore water bodies.

The accuracy of the coastline extracted results by different indices at low tide and high tide were different, leading to very different results for coastline extraction. The silty mudflats are revealed at low tide, and the classification results for *NDWI* and *AWEI* were incorrect, leading to a decrease in coastline extraction accuracy. For example, the *NDWI* identified part of the water with high sediment content in the overlapping area of Figure 1a,b as land and water bodies, respectively, while it identified part of the coastal land in the overlapping area of Figure 1b,c as water bodies and land, respectively. Silty mudflats have different states under different tidal conditions, and the accurate extraction of information on silty mudflats under various scenarios is critical to the correct extraction

of coastlines. Ryu et al. [23] used the red band density partitioning to extract the waterline of silty mudflats in Gomso Bay, Korea, with an average deviation of less than 60 m. Tong et al. [39] explored the *NDWI* and ratio of the green band to short-wave infrared band 1 in different seasons to extract the shoreline of silty mudflats in northern Vietnam. The results showed that different uses of the green band divided by short-wave infrared band 1 with coefficients of variation of 13% in the dry season and 25% in the rainy season was the optimal shoreline extraction method. In summary, the *IWI* evaluated in one pixel with an accuracy of more than 81% in various cases can be better applied to a wide range of situations.

However, the spatial resolution difference between the shoreline extracted from sentinel-2 10 m MSS image and landsat-8 30 m image was small. The analysis would be improved if more accurate images could be acquired for verification.

6. Conclusions

The *IWI* spectral water index constructed in this study uses the blue, green, SWIR1 and SWIR2 bands of the OLI sensor to improve the accuracy of complex coastline extraction. The results demonstrate that it performs better than the other commonly used indices, such as the *NDWI, MNDWI* and *AWEI*. In particular, the proposed *IWI* index can better identify offshore artificial structures and silty mudflats than the commonly used spectral indices with higher accuracy. In addition, the *IWI* method allows the extraction of coastlines from shores with different tidal conditions and different land covers (e.g., wetlands, buildings, etc.) with better accuracy. It can be extended to a wide range of complex coastal types without being restricted to specific conditions (e.g., micro-tidal or single coastal types).

The results show that the *IWI* is independent of tides and the sand content of the water column, reduces the "salt-and-pepper" phenomenon of Otsu's classification, accurately identifies water boundary information, extracts information on silty mudflats and offshore structures with high accuracy and significantly increases coastline extraction automation. The *IWI* combined with the Otsu algorithm extracts multiple types of coastlines, and it has been verified that the one-pixel accuracy of the extracted muddy coastline exceeds 84%, while the three-pixel accuracy exceeds 91%. It is reliable and can be used for an improved understanding of sea–land processes and coastline evolution.

Author Contributions: Conceptualization, W.T.; methodology, C.Z.; software, J.L.; validation, W.T., C.J.; formal analysis, G.Z.; investigation, J.Z.; resources, X.P.; data curation, X.H.; writing—original draft preparation, W.T.; writing—review and editing, J.Z.; visualization, J.L.; supervision, C.Z.; project administration, C.Z.; funding acquisition, C.Z. All authors have read and agreed to the published version of the manuscript.

Funding: This research was funded by the National Natural Science Foundation of China grant number 42130405 and the Innovative and Entrepreneurial Talent Program of Jiangsu Province grant number R2020SC04.

Acknowledgments: We are grateful to those involved in data processing and manuscript writing revision.

Conflicts of Interest: The authors declare no conflict of interest.

References

1. Wu, T.; Hou, X.Y. Review of research on coastline changes around the world. *Acta Ecol. Sin.* **2016**, *36*, 1170–1182.
2. Louati, M.; Saïdi, H.; Zargouni, F. Shoreline change assessment using remote sensing and GIS techniques: A case study of the Medjerda delta coast, Tunisia. *Arab. J. Geosci.* **2015**, *8*, 4239–4255.
3. Chen, Y.; Dong, J.W.; Xiao, X.M.; Zhang, M.; Tian, B.; Zhou, Y.X.; Li, B.; Ma, Z.J.Land claim and loss of tidal flats in the Yangtze Estuary. *Sci. Rep.* **2016**, *6*, 24018.
4. Wu, Y.Q.; Liu, Z.L. Research progress on methods of automatic coastline extraction based on remote sensing images. *J. Remote Sens.* **2019**, *23*, 582–602.

5. Shi, J.J.; Li, W.F.; Liu, Y.L.; Zhou, W.Q.; Han, L.J.; Tian, S.F.; Wang, Y.M.; Niu, X.Q. Impacts of urbanization on coastline and coastal zone in the Guangdong-Hong Kong-Macao Greater Bay Area. *Acta Ecol. Sin.* **2022**, *1*, 1–10.
6. Zhang, X.X.; Yan, C.Q.; Xu, P.; Dai, Y.X.; Yan, W.B.; Ding, X.R.; Zhu, C.X.; Mei, D.D. Historical evolution of tidal flat reclamation in the Jiangsu coastal areas. *Acta Geogr. Sin.* **2013**, *68*, 1549–1558.
7. Ma, X.F.; Zhao, D.Z.; Xing, X.G.; Zhang, F.S.; Wen, S.Y.; Yang, F. Means of with drawing coastline by remote sensing. *Mar. Environ. Sci.* **2007**, *26*, 185–189.
8. Li, Q.Q.; Lu, Y.; Hu, S.B.; Hu, Z.W.; Li, H.Z.; Liu, P.; Shi, T.Z.; Wang, C.S.; Wang, J.J.; Wu, G.F. Review of remotely sensed geo-environmental monitoring of coastal zones. *J. Remote Sens.* **2016**, *20*, 1216–1229.
9. Yan, Z.; Jin-wei, D.; Xiang-ming, X.; Tong, X.; Zhi-qi, Y.; Guo-song, Z.; Zhen-hua, Z.; Yuan-wei, Q. Open Surface Water Mapping Algorithms: A Comparison of Water-Related Spectral Indices and Sensors. *Water* **2017**, *9*, 256–256.
10. Zhou, Z.; Gui, S.X.; Li, Y.C.; Tao, Y.Q.; Peng, Y. Inversion of typical water quality parameters in Chaohu Lake based on composite spectral indices. *Yangtze River* **2020**, *51*, 45–50.
11. Li, Y.M.; Zhang, X.J. Remote Sensing Monitoring of Leaf Water Contentin Lycium Barbarum Based on Spectral Index. *Geogr. Geo-Inf. Sci.* **2019**, *35*, 16–21.
12. McFeeters, S.K. The use of the Normalized Difference Water Index (NDWI) in the delineation of open water features. *Int. J. Remote Sens.* **1996**, *17*, 1425–1432.
13. Xu, H.Q. A Study on Information Extraction of Water Body with the Modified Normalized Difference Water Index (MNDWI). *J. Remote Sens.* **2005**, *9*, 589–595.
14. Cao, R.L.; Li, C.J.; Liu, L.Y.; Wang, J.H.; Yan, G.J. Extracting Miyun reservoir's water area and monitoring its change based on a revised normalized different water index. *Sci. Surv. Mapp.* **2008**, *33*, 158–160.
15. Yan, P.; Zhang, Y.J.; Zhang, Y. A Study on Information Extraction of Water System in Semi-arid Regions with the Enhanced Water Index (EWI) and GIS Based Noise Remove Techniques. *Remote Sens. Inf.* **2007**, *6*, 62–67.
16. Feyisa, G.L.; Meilby, H.; Fensholt, R.; Proud, S.R. Automated Water Extraction Index: A new technique for surface water mapping using Landsat imagery. *Remote Sens. Environ.* **2014**, *140*, 23–35.
17. Sheng, J.H.; Zhang, C.; Wan, J.H. Automatic coastline extraction method based on multitemporal remote sensing data. *Mar. Sci.* **2021**, *45*, 16–22.
18. Borja, S.P.V.; Miguel, O.S. Automatic methodology to detect the coastline from landsat images with a new water index assessed on three different spanish mediterranean deltas. *Remote Sens.* **2019**, *11*, 44.
19. Yun, D.; Zhang, Y.; Feng, L.; Wang, Q.; Li, W.; Li, X. Water bodies' mapping from sentinel-2 imagery with modified normalized difference water index at 10-m spatial resolution produced by sharpening the swir band. *Remote Sens.* **2016**, *354*, 354.
20. Wu, J.P.; Zhang, Y.; Zhang, J.; Fan, S.L.; Yang, C.; Zhang, X.F. Comparison and analysis of water indexes in muddy coasts based on MODIS data: A case study of the Yellow River Delta coast. *Remote Sens. Land Resour.* **2019**, *31*, 242–249.
21. Zhang, X.; Wang, X.P.; Huang, A.Q.; Li, Y.S.; Zhang, S.; Bai, Y.; Malak, H.; Zhang, J.H. Extraction of complex coastline feature and its multi-year changes in Shandong Peninsula Based on remote sensing image. *Trans. Oceanol. Limnol.* **2021**, *43*, 171–181.
22. Paravolidakis, V.; Ragia, L.; Moirogiorgou, K.; Zervakis, M.E. Automatic coastline extraction using edge detection and optimization procedures. *Geosciences* **2018**, *8*, 407.
23. Ryu, J.H.; Won, J.S.; Min, K.D. Waterline extraction from Landsat TM data in a tidal flat: A case study in Gomso Bay, Korea. *Remote Sens. Environ.* **2002**, *83*, 442–456.
24. Ding, X.R.; Kang, Y.Y.; Mao, Z.B.; Sun, Y.L.; Li, S.; Gao, X.; Zhao, X.X. Analysis of largest tidal range in radial sand ridges southern Yellow Sea. *Acta Oceanol. Sin.* **2014**, *36*, 12–20. (In Chinese)
25. Zhang, X.X.; Wang, W.W.; Yang, C.Q.; Yan, W.B.; Dai, Y.X.; Xu, P.; Zhu, C.X. Historical Coastline Spatio-temporal Evolution Analysis in Jiangsu Coastal Area During the Past 1000 Years. *Sci. Geogr. Sin.* **2014**, *34*, 344–351.
26. Chen, W.T.; Zhang, D.; Shi, S.J.; Zhou, J.; Kang, M. Research on monitoring coastline changes by remote sensing in muddy coast, central Jiangsu coast. *HaiyangXuebao* **2017**, *39*, 138–148.
27. Otsu, N. A threshold selection method from gray-level histograms. *IEEE Trans. Syst. Man Cybern.* **1979**, *9*, 62–66.
28. Wang, Y.X.; Liu, Y.X.; Jin, S.; Sun, C.; Wei, X.L. Evolution of the topography of tidal flats and sandbanks along the Jiangsu coast from 1973 to 2016 observed from satellites. *ISPRS J. Photogramm. Remote Sens.* **2019**, *150*, 27–43.
29. Chen, W.T.; Zhang, D.; Cui, D.D.; Lv, L.; Xie, W.J.; Shi, S.J.; Hou, Z.Y. Monitoring spatial and temporal changes in the continental coastline and the intertidal zone in Jiangsu province, China. *Acta Geogr. Sin.* **2018**, *73*, 1365–1380.
30. Li, Y.F.; Liu, H.Y.; Sun, X.B.; Zhu, L.J. Assessment of ecological functions for coastal wetlands based on hydrogeomorphic units: A case study on coastal wetland of Yancheng, Jiangsu Province, China. *Acta Ecol. Sin.* **2010**, *30*, 1718–1724.
31. Liao, H.J.; Li, G.S.; Wang, S.H.; Cui, L.L.; OuYang, N.L. Evolution and spatial patterns of tidal wetland in North Jiangsu Province in the past 30 Years. *Prog. Geogr.* **2014**, *33*, 1209–1217.
32. USGS. Product Guide: Landsat 8 Surface Reflectance Code (LaSRC) Product. Available online: https://www.usgs.gov/media/files/landsat-8-collection-1-land-surface-reflectance-code-product-guide (accessed on 18 January 2022).
33. Roy, D.P.; Qin, Y.; Kovalskyy, V.; Vermote, E.F.; Ju, J.; Egorov, A.; Hansen, M.C.; Kommareddy, I.; Yan, L. Conterminous United States demonstration and characterization of MODIS-based Landsat ETM+ atmospheric correction. *Remote Sens. Environ.* **2014**, *140*, 433–449.

34. Xu, H.Q.; Tang, F. Analysis of new characteristics of the first Landsat 8 image and their eco-environmental significance. *Acta Ecol. Sin.* **2013**, *33*, 3249–3257.
35. Xu, H.Q. Water colour variation analysis of the coastal waters surrounding Xiamen Island of SE China by multispectral and multitem poral remote sensing measurements. *Acta Sci. Circumstantiae* **2006**, *26*, 1209–1218.
36. Tang, K.K.W.; Mahmud, M.R. Imagery-derived bathymetry in Strait of Johor's turbid waters using multispectral images. *Remote Sens. Spat. Inf. Sci. ISPRS Arch* **2018**, *42*, 133–137.
37. Zhang, J.; Lai, Z.L.; Sun, J. Coastline extraction of remote sensing image by combining Otsu, regional growth method with morphology. *Bull. Surv. Mapp.* **2020**, *10*, 89–92.
38. Hou, X.Y.; Wu, T.; Hou, W.; Chen, Q.; Wang, Y.D.; Yu, L.J. Characteristics of coastline changes in mainland China since the early 1940s. *Sci. China Earth Sci.* **2016**, *46*, 1065–1075.
39. Tong, S.S.; Deroin, J.P.; Pham, T.L. An optimal waterline approach for studying tidal flat morphological changes using remote sensing data: A case of the northern coast of Vietnam. *Estuarine. Coast. Shelf Sci.* **2020**, *236*, 106613.